

## Article

# Experimental Study on the Compressive and Shear Mechanical Properties of Cement–Formation Interface Considering Surface Roughness and Drilling Mud Contamination

Lei Wang <sup>1</sup>, Bohang Liu <sup>1,2,\*</sup>, Hanzhi Yang <sup>3</sup>, Yintong Guo <sup>1</sup>, Jing Li <sup>2</sup> and Hejuan Liu <sup>1</sup>

<sup>1</sup> State Key Laboratory of Geomechanics and Geotechnical Engineering, Institute of Rock and Soil Mechanics, Chinese Academy of Sciences, Wuhan 430071, China

<sup>2</sup> School of Pipeline and Civil Engineering, China University of Petroleum (East China), Qingdao 266580, China

<sup>3</sup> State Key Laboratory of Coal Mine Disaster Dynamics and Control, Chongqing University, Chongqing 400044, China

\* Correspondence: z20060067@s.upc.edu.cn; Tel.: +86-18571513966 or +86-027-87198651

**Abstract:** In a casing-cement sheath-formation system, the cement–formation interface is usually weakly cemented for the residual of drilling mud, in which a leakage path would easily form, threatening the safe operation of underground energy exploitation and storage. To evaluate the compressive and shear mechanical behavior of the cement–formation interface, cement–rock composite cylindrical specimens were prepared. Uniaxial and triaxial compression and direct shear tests were implemented. The flushing efficiency of the rock surface, compressive strength, interface incompatible deformation, parameters of shear strength, and morphology of shear failure surface were acquired and analyzed. Results show that the flushing efficiency of shale surface decreases from 76.7% to 64.2% with the surface roughness increasing from 0 to 2 mm. The flushing efficiency of sandstone is only 44.7%, remarkably lower than that of shale. With the stress condition transforming from uniaxial to triaxial compression, the feature of the stress–strain curves changes from elastic-brittle to elastoplastic, and the compressive strength increases from 20.6~60.1 MPa to 110~120 MPa. The cement part presents noteworthy plastic deformation and several micro shear fractures develop. There is incompatible deformation between cement and rock, which induces interface debonding for almost all the composite specimens. The internal friction angle and cohesive strength both decrease with the increase in pollution degree of drilling mud, and increase with the rise in surface roughness. The shear failure surface is not exactly the rock–cement interface, but usually manifests as a shear zone, in which the rock, cement, and interface all contribute to the final shear failure. The above findings would be valuable for the revealing of cement–formation interface failure mechanism.

**Keywords:** cement–rock interface; drilling mud pollution; flushing efficiency; compressive strength; incompatible deformation; interface shear parameters



**Citation:** Wang, L.; Liu, B.; Yang, H.; Guo, Y.; Li, J.; Liu, H. Experimental Study on the Compressive and Shear Mechanical Properties of Cement–Formation Interface Considering Surface Roughness and Drilling Mud Contamination. *Energies* **2022**, *15*, 6472. <https://doi.org/10.3390/en15176472>

Academic Editor: Hossein Hamidi

Received: 6 July 2022

Accepted: 2 September 2022

Published: 5 September 2022

**Publisher's Note:** MDPI stays neutral with regard to jurisdictional claims in published maps and institutional affiliations.



**Copyright:** © 2022 by the authors. Licensee MDPI, Basel, Switzerland. This article is an open access article distributed under the terms and conditions of the Creative Commons Attribution (CC BY) license (<https://creativecommons.org/licenses/by/4.0/>).

## 1. Introduction

A wellbore is an artificial established channel connecting the surface and deep formations in underground energy exploitation [1–5] and storage [6–10]. The cementing operation is implemented after drilling. As shown in Figure 1a, before injecting cement slurry, flushing fluid is pumped into the well to clean the hole and separate mud from cement [11]. Then, the cement slurry is pumped in and placed around the lower part of the casing. After the setting and hardening of the cement, a robust and tight casing–cement–formation sealing system is formed (Figure 1b).

As it is affected by various engineering disturbances after cementing (such as hydraulic fracturing, temperature alteration, cyclic injection–production, etc.), the loss of annular isolation happens in three positions: (1) the body of the cement sheath, (2) the casing–cement interface (the first interface), and (3) the cement–formation interface (the second interface) [12,13]. The mechanical behavior and failure mechanism of oil cement stone were

systematical investigated [14–18]. The casing–cement interface is similar to the structure of steel concrete, which usually forms good cementation. Among the three locations, the cement–formation interface is in the most complex environment. On the one hand, the wellbore wall is naturally undulating. When encountering a broken formation, the wellbore wall becomes rougher. On the other hand, drilling mud easily adheres to the grooves of the wellbore, and is not completely removed (Figure 1c). The residual drilling mud impedes the cementation between the cement and the formation. Therefore, the second interface is naturally weakly cemented, and there is a high risk of a leakage path forming.

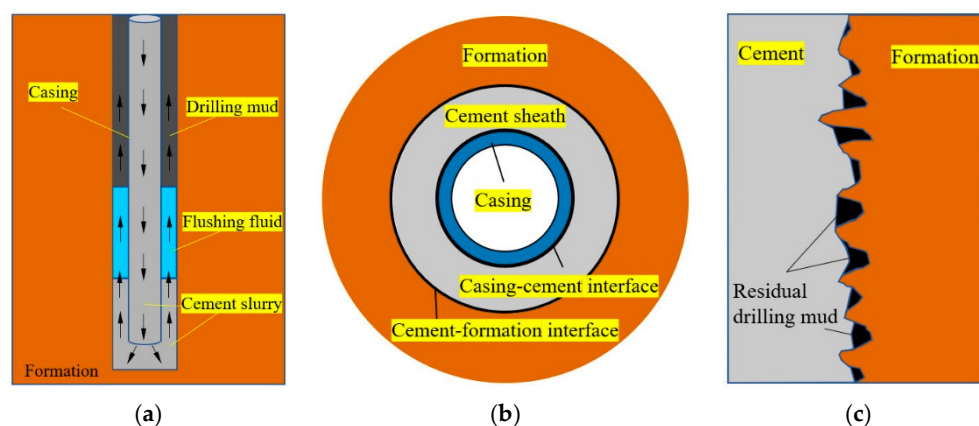


**Figure 1.** Primary cementing and casing–cement–formation system. (a) Primary cementing, (b) Casing–cement–formation structure, (c) Cement–formation interface.

A review of the literature shows that previous studies on the mechanical properties of cement–formation interfaces are relatively few and limited. Opedal et al. [12] argued that the presence of drilling fluid and drilling fluid type were crucial parameters for cement–formation bonding. Ladva et al. [19] found that the presence of filter cakes on the permeable sandstone could decrease the interface shear bond strength from 120 psi to 0.1–1 psi. Plank et al. [20] used synthetic ceramic core samples to simulate reservoir rock, and tested the bonding strength of the cement–formation interface containing mudcake. Liu et al. [21] measured the shear bond strength of the cement–shale interface using a new method, but the interface roughness and drilling fluid residual were ignored. Lian et al. [22] studied the cement-to-formation interface debonding by a numerical method, but the interface roughness was not considered.

The above research mainly tested the shear strength of the cement–formation interface without considering the action of normal stress. However, in underground situation, the cement–formation interface is suppressed by normal stress, which influences the shear behavior of the interface according to the Mohr–Coulomb criterion. A direct shear test, considering multiple normal stress levels, would be a good choice. The obtained shear strength parameters (internal friction angle and cohesive strength) would provide a more comprehensive evaluation of the interface shear behavior. In addition, the deformation characteristics near the interface under compression are also rarely involved, which could reveal the interface debonding mechanism.

In this study, cement–rock composite cylindrical specimens were prepared considering the interface roughness and drilling mud residue to simulate the cement–formation interface in a wellbore system. The flushing efficiency of the rock surface suffering under drilling mud pollution and flushing fluid washing was calculated. The compressive strength of cement–rock specimens and interface incompatible deformation characteristics were acquired under uniaxial and triaxial states. The parameters of shear strength and morphology of shear failure surfaces were analyzed. The results are valuable for the understanding of the cement–formation interface failure mechanism.

## 2. Materials and Test Methods

### 2.1. Sample Preparation

To investigate the compressive and shear mechanical property of the cement–formation interface, rock–cement composite specimens were designed. Shale and sandstone were selected as the rock part. Specifically, shale was collected from the outcrop of the Longmaxi Formation in Sichuan Basin [23,24], which was the target reservoir of shale gas, while sandstone was gathered from the Yanchang Formation in Ordos Basin [25], the producing area of tight sandstone gas. The basic mechanical parameters and mineral composition of these two types of rock are listed in Tables 1 and 2, respectively. Oil well cement was adopted to make the cement part. Class-G oil well cement (100%), water (40%), fluid loss additive (4%), and defoaming agents (0.25%) were mixed to form the cement slurry.

**Table 1.** Basic mechanical parameters of selected rock and cement stone.

Materials	Uniaxial Compression Strength (MPa)	Young's Modulus (GPa)	Poisson's Ratio	Brazilian Tensile Strength (MPa)
Rock–shale	98.5	24.10	0.20	13.0
Rock–sandstone	41.2	6.23	0.13	4.4
Cement stone	59.3	9.85	0.15	3.2

Notes: each parameter in the table is the average value of 3–5 data. The parameters of cement stone were tested after curing of 28 days.

**Table 2.** Mineral composition of selected shale and sandstone.

Rock Type	Minerals (%)								
	Quartz	Albite	Calcite	Dolomite	Pyrite	Illite	Microcline	Clinochlore	
Shale	69.78	11.40	2.80	2.16	2.93	10.93	–	–	
Sandstone	20.19	15.65	47.76	2.01	–	–	8.56	5.83	

The preparation procedure is presented in Figure 2. Firstly, the standard rock cylinder (height of 100 mm and diameter of 50 mm) was cut along its central section with diamond wire saw (Figure 2a). The setting of cutting path is specially introduced in the following part. Three types of surface roughness were designed (Figure 3): (1) flat surface (roughness 0 mm), which simulated the ideal smooth state of the wellbore wall; (2) small undulating surface (roughness 1 mm) (Figure 3a), in which the cutting path was a zigzag line with amplitude of 1 mm, which was a simplified simulation of the roughness condition of real wellbore wall; and (3) large undulating surface (roughness 2 mm) (Figure 3b), which was prefabricated by a zigzag cutting path with amplitude of 2 mm; the wall of the broken formation exhibited greater roughness.

Then, as shown in Figure 2b, oil-based drilling mud, with volume of 15 mL, was poured on the cutting surface of the rock. After precipitation of 6 h, the drilling mud was poured out. Immediately, the polluted surface was immersed into the flushing fluid (15 mL). The residual drilling mud was dissolved and washed away. The drilling mud and flushing fluid were taken from the site. During the mud pollution and flushing process, the mass variation of the rock specimens was recorded, to acquire the flushing efficiency, which was calculated using

$$\eta_f = \frac{m_1 - m_2}{m_1 - m_0} \times 100\% \quad (1)$$

where  $m_0$  is the initial mass of the rock specimen;  $m_1$  is the mass after precipitation and pouring out of the drilling mud; and  $m_2$  is the mass after flushing fluid washing.

Finally, the rock was placed into the mould, with the treated face up. Mixed cement slurry was poured into it. Demolding occurred after curing of 72 h and continue curing for 28 days. After cutting and polishing of the cement surface, the rock–cement composite specimens (standard cylinder  $\phi 50 \times 100$  mm) were ready to test (Figure 2c).

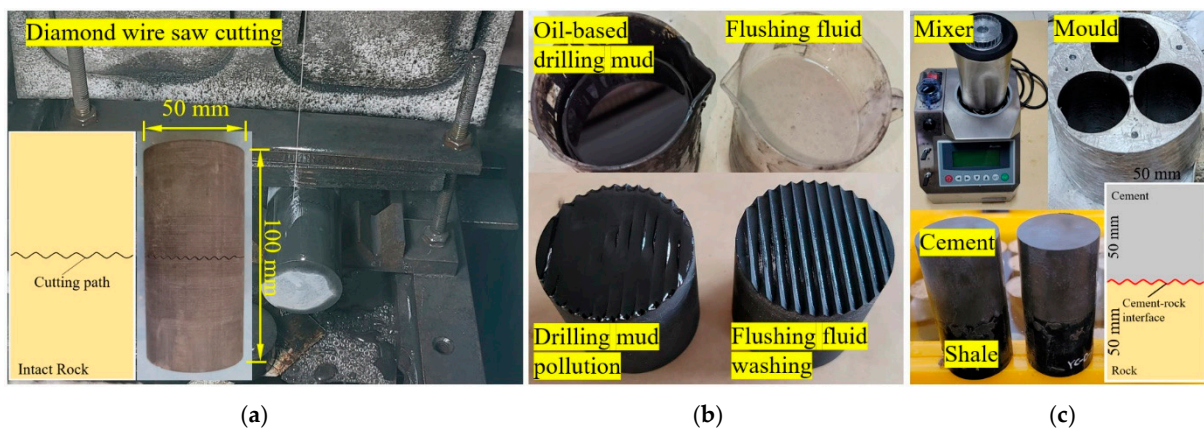
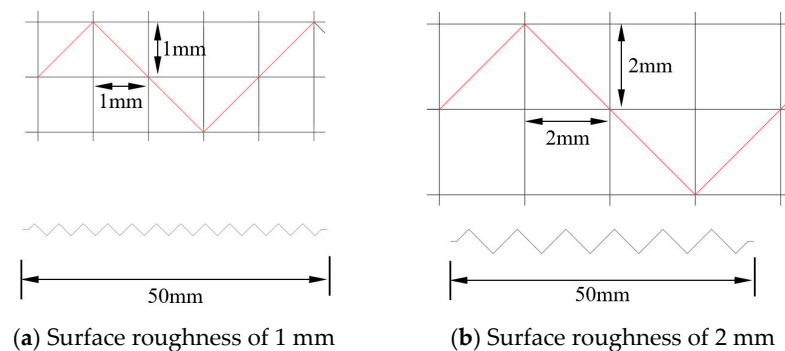
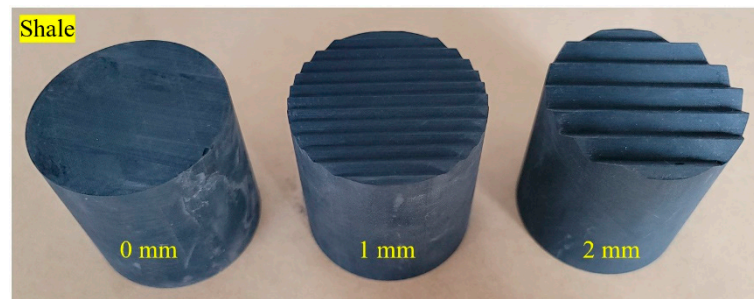


**Figure 2.** Preparation steps of rock–cement composite specimens. (a) Cutting rock with diamond wire saw, (b) Rock surface pollution and flushing, (c) Cement pouring and curing.



(a) Surface roughness of 1 mm

(b) Surface roughness of 2 mm



(c) Prepared shale with different roughness

**Figure 3.** Roughness setting of rock surface.

## 2.2. Experimental Design

Based on the above description of sample preparation, we designed five types of rock–cement composite specimens (Table 3), considering key factors of lithology, interface roughness, and interface cleanliness. Compression and shear tests were implemented on each type of rock–cement specimens. In compression tests, uniaxial compression was firstly conducted, which also provided reference for the setting of normal stress in subsequent shear experiments. Then, triaxial compression was performed under the confining pressure of 20 MPa. The above two types of compression tests were all controlled by axial displacement, with a constant rate of 0.12 mm/min, and the complete stress–strain curves were recorded. The objective of the compression tests was to investigate the deformation and failure characteristic of the rock–cement interface under compression. The confining pressure of 0 MPa (uniaxial) and 20 MPa (triaxial) were designed to simulate the stress states at shallow and deep formations, respectively.

**Table 3.** Experimental scheme.

Composite Type	Interface Roughness (mm)	Interface Pollution and Flushing	Sample Number	
			Compression Test	Shear Test
Shale + Cement	0	Drilling mud (15 mL)	YC-0-2-(1, 2)	YS-0-2-(1, 2, 3, 4)
	1	+	YC-2-2-(1, 2)	YS-2-2-(1, 2, 3, 4)
	2	Flushing fluid (15 mL)	YC-4-2-(1, 2)	YS-4-2-(1, 2, 3, 4)
	1	Fresh and untreated	YC-2-0-(1, 2)	YS-2-0-(1, 2, 3, 4)
	1	Drilling mud (15 mL)	YC-2-3-(1, 2)	YS-2-3-(1, 2, 3, 4)
Sandstone + Cement	1	Drilling mud (15 mL)	SC-2-2-(1, 2)	SS-2-2-(1, 2, 3, 4)
		+		
		Flushing fluid (15 mL)		

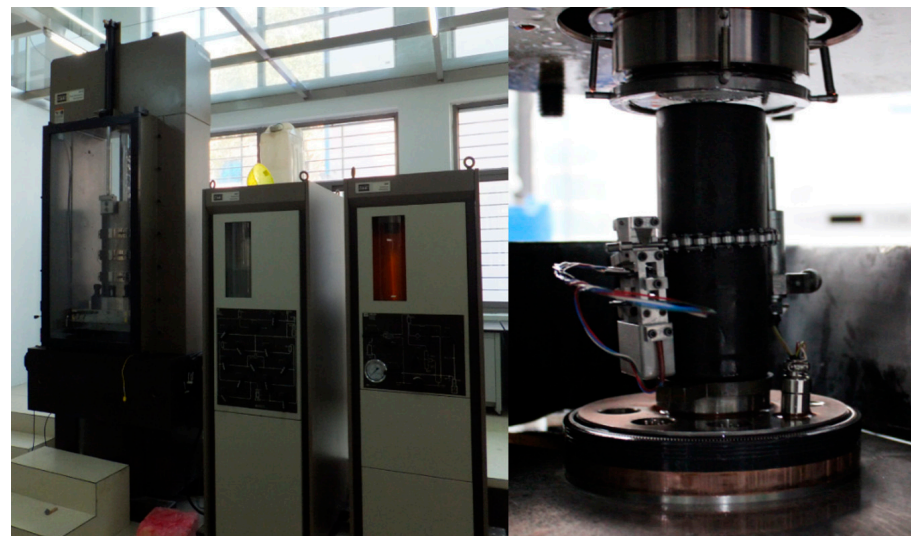
After compression tests, direct shear experiments were carried out to reveal the shear behavior and failure mechanism of the rock–cement interface. Based on the results of uniaxial compression, the normal stresses in shear tests were determined. The principle is that the specimen should be in a linear elastic state during the process of vertical loading. The general test processes are: (1) place the specimen in the shear box; (2) apply the normal force on the top to the pre-set value; and (3) exert shear force on the specimen in horizontal direction until failure [26]. Here, the normal force was loaded at a constant rate of 1 kN/s, and shear force was applied by the control of horizontal shear displacement, at the rate of 0.002 mm/s. Four levels of normal stresses were set, and the corresponding values of shear strength were acquired. According to the theory of Mohr–Coulomb [27], the formula of shear strength was determined by the linear fit of the four scatters.

$$\tau = \sigma_n \tan \varphi + c \quad (2)$$

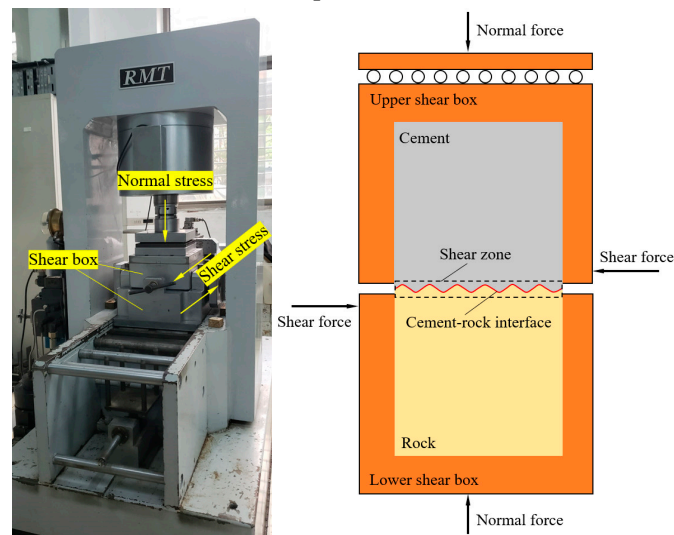
where  $\tau$  is the shear strength at a given normal stress, MPa;  $\sigma_n$  is the normal stress, MPa, which remained unchanged during shear loading;  $\varphi$  is the internal friction angle, °; and  $c$  is the cohesive strength, MPa.

### 2.3. Experimental Equipment

The uniaxial and triaxial compression experiments were performed on an MTS 815 test system [28]. It provided a maximum axial force of 4600 kN and confining pressure of 140 MPa, with excellent rigidity of  $11.0 \times 10^9$  N/m (Figure 4a). The direct shear tests were conducted on a RMT-150C rock mechanics testing system [26] (Figure 4b), which was self-developed by the Wuhan Institute of Rock and Soil Mechanics, Chinese Academy of Sciences (WHRSM, CAS). The maximum horizontal shear and vertical compressive forces reach 400.0 and 1000.0 kN, respectively. The control rate of displacement could be set between 0.0001 and 1.0 mm. The rigidity of the whole frame is  $5.0 \times 10^9$  N/m.



(a) MTS815 for compression tests



(b) RMT-150C for direct shear tests

**Figure 4.** Test system for compression and direct shear experiments.

### 3. Experimental Results and Analysis

#### 3.1. Mud Flushing Efficiency of Rock Surface

As shown in Figure 5, after drilling mud pollution and deposition, the grooves of the rock surface are filled with drilling mud. With the treatment of flushing fluid washing, most of the attached mud on the shale surface is removed. The buried undulating surface reappears. However, after careful observation, we could still see a little mud and flushing fluid remaining in the bottom of the grooves. In comparison, the residual drilling mud on the sandstone surface is quite difficult to clean. After the same flushing treatment of shale, there is still much drilling mud left and filling the grooves. We could hardly see the clean sandstone surface reappear.

The flushing efficiency could be used to quantitatively evaluate the washing effect. As shown in Figure 6, the flushing efficiency decreases from 76.7% to 64.2%, with the surface roughness increasing from 0 mm to 2 mm. As it is difficult to wash away the drilling mud hiding in the depths of the rock grooves, under the same cleaning procedure, the flushing efficiency of sandstone is only 44.7%, remarkably lower than that of shale (68.7%).



Figure 5. Rock surface state with different treatment method.

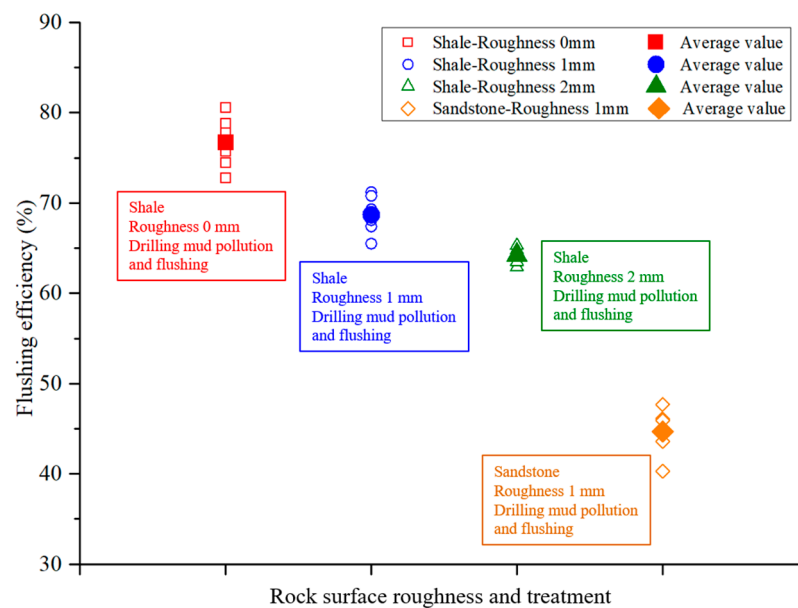
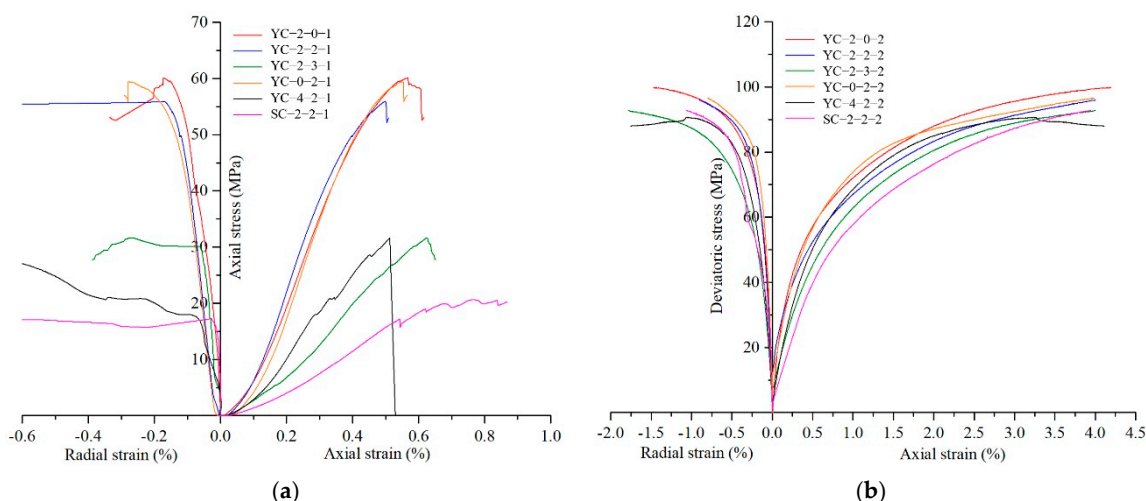


Figure 6. Flushing efficiency of rock surface with difference roughness and lithology.

### 3.2. Mechanical Behavior of Rock–Cement Specimen in Compression

#### (1) Compressive strength

In the uniaxial compression state, the values of compressive strength vary in a wide range, influenced jointly by interface cleanliness, roughness, and lithology. As depicted in Figure 7a, shale–cement specimens with good interface cleanliness and small roughness (YC-2-0-1, YC-0-2-1, YC-2-2-1) show relatively high strength (55.9~60.1 MPa). The reason is that good interface cleanliness brings strong interface bonding, and small roughness does not induce excessive stress concentration at the interface. Therefore, the shale–cement specimen, as a solid whole, can bear a relatively high compressive stress. Under the condition of drilling mud pollution without flushing, the shale–cement interface is poorly cemented for the large amount of residual drilling mud. Therefore, relatively free lateral slippage can happen between cement and shale at the interface. The overall stiffness of the shale–cement specimen declines and the corresponding compressive strength decreases. Specifically, the compressive strength of specimen YC-2-3-1 is only 31.7 MPa. For the specimen with the interface roughness of 2 mm (YC-4-2-1), the value of compressive strength is only 31.6 MPa. The high level of roughness inducing excessive stress concentration at the interface is the main reason. The compressive strength of the sandstone–cement specimen (SC-2-2-1) is the weakest, which is only 20.6 MPa. Poor interface cementation and low strength of sandstone contributes to the low bearing capacity of the composite specimen.



**Figure 7.** Stress–strain curves of composite rock–cement specimens under uniaxial and triaxial compression. (a) Stress–strain curves under uniaxial compression, (b) Stress–strain curves under triaxial compression.

The situation is quite different for specimens under triaxial compression. At the confining pressure of 20 MPa, all stress–strain curves exhibit remarkable elastoplastic characteristics (Figure 7b), which is different from the elastic–brittle feature under uniaxial compression. The values of the compressive strengths are very close, and focus on the range of 110~120 MPa (Table 4). The existence of confining pressure inhibits the adverse effects of poor interface cementation and roughness on compressive strength.

**Table 4.** Data collection of compressive strengths.

Test Type	Sample No.	Compressive Strength (MPa)	Test Type	Sample No.	Deviatoric Stress (MPa)	Compressive Strength (MPa)
Uniaxial compression	YC-2-0-1	60.1	Triaxial compression ( $\sigma_3 = 20$ MPa)	YC-2-0-2	99.8	119.8
	YC-2-2-1	55.9		YC-2-2-2	95.9	115.9
	YC-2-3-1	31.7		YC-2-3-2	92.8	112.8
	YC-0-2-1	59.4		YC-0-2-2	96.5	116.5
	YC-4-2-1	31.6		YC-4-2-2	90.7	110.7
	SC-2-2-1	20.6		SC-2-2-2	92.6	112.6

Note: Triaxial compressive strength = deviatoric stress + confining pressure.

(2) Failure mode

By observing the specimens after tests, we could obtain the failure mode and evaluate the interface cementation integrity (Figure 8). Under the condition of uniaxial compression ( $\sigma_3 = 0$  MPa), tensile splitting in a vertical direction is the dominate failure mode. Fractures usually initiate at the relatively weak part (cement or sandstone), and propagate across the interface to the strong part (shale). However, the integrity of the interface cementation differs according to the interface cleanliness and roughness. As the degree of interface pollution increases, the post-test interface integrity changes from bonding (Figure 8a) to partial bonding (Figure 8b), and to debonding (Figure 8c). Due to the large amount of residual drilling mud and vertical compressive loading, drilling mud extrudes from the interface in specimen YC-2-3-1 (Figure 8c). With the increase in interface roughness (0 → 1 → 2 mm), the integrity of the interface cementation also evolves from bonding to debonding (Figure 8b,d,e). For the specimen (YC-4-2-1) with interface roughness of 2 mm (Figure 8e), it is worth noting that fractures initiate at peak points of the convex zone, which is the result of stress concentration and corresponds to the relatively low compressive strength. The sandstone–cement specimen also shows interface debonding. Based on the

above analysis, it is demonstrated that interface debonding under uniaxial compression appears in specimens with excessive mud residue and poor interface cementation.



**Figure 8.** Deformation and failure characteristics of composite rock–cement specimens under uniaxial and triaxial compression. (a) YC-2-0-(1, 2), Roughness 1 mm, Fresh and untreated surface, (b) YC-2-2-(1, 2), Roughness 1 mm, Drilling mud contamination and flushing, (c) YC-2-3-(1, 2) Roughness 1 mm, Drilling mud contamination without flushing, (d) YC-0-2-(1, 2), Roughness 0 mm, Drilling mud contamination and flushing, (e) YC-4-2-(1, 2), Roughness 2 mm, Drilling mud contamination and flushing, (f) SC-2-2-(1, 2), Roughness 1 mm, Drilling mud contamination and flushing.

In triaxial compression with a confining pressure of 20 MPa, the deformation of all composite specimens is similar. The cement part presents noteworthy plastic deformation, with middle domain swelling, and several micro shear fractures develop (Figure 8). The rock parts almost remain good integrity. Due to the excessive compressive deformation of cement in the vertical direction, the lateral expansion is also very large, while the lateral deformation of rock is relatively small. There is severe incompatible deformation of cement– and rock-induced interface debonding for nearly all composite specimens under triaxial

compression. In the neighborhood of the interface, locally fractured cement is spotted in specimens YC-2-2-2 and YC-2-3-2 (Figure 8b,c,e), because the cement at the interface is not in an ideal compact structure and has relatively low strength. In addition, stress concentration, induced by high levels of surface roughness, also influences the failure of cement. As shown in Figure 8b,e,f, several inclined shear fractures intersect with the peak points of the convex zone at the rough interface. Therefore, the failure mode of interface debonding and local cement fracturing should be paid more attention for the cement–rock interface under a triaxial compressive state.

### 3.3. Shear Behavior of Rock–Cement Interface

The scatters of shear and normal stress are plotted in Figure 9. For each type of composite specimens, shear stress keeps growing with the increase in normal stress. Based on the Mohr–Coulomb criterion, the linear fit was implemented, and parameters of shear strength (internal friction angle and cohesive strength) acquired are shown in Table 5.

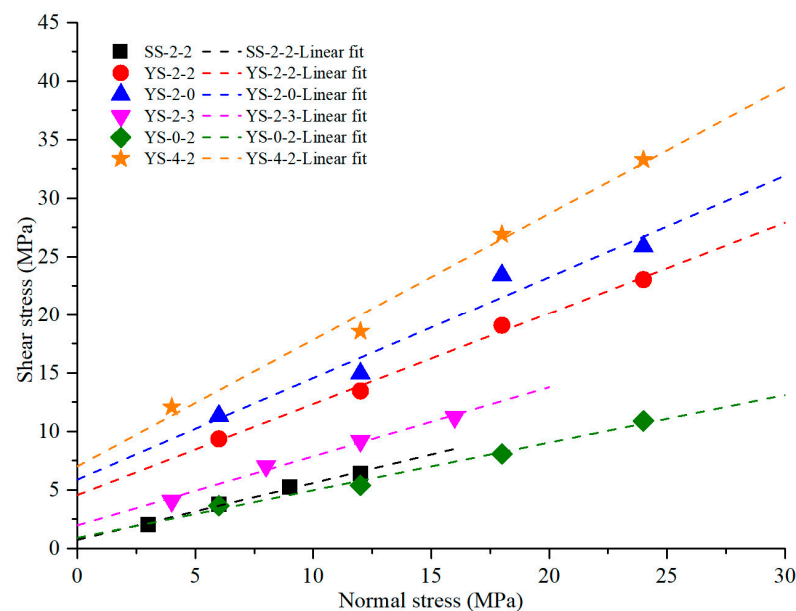


**Figure 9.** Scatters of shear and normal stresses and corresponding linear fit curves.

The tangent value of the internal friction angle ( $\tan\phi$ ) is the slope of the fitted line, which reflects the sliding friction property of the shear plane, and is determined by surface roughness and material stiffness. As shown in Figure 10a, the values of internal friction angle decrease with the increase in drilling mud pollution for shale–cement specimens with the same surface roughness of 1 mm. For specimens with fresh and untreated surfaces, the internal friction angle is  $40.9^\circ$ , while it decreases to  $37.9^\circ$  for surface treated with drilling mud pollution and flushing fluid washing. If the step of flushing is further removed, the value continues to decline to  $30.6^\circ$ . Under the same condition of surface cleanliness, the internal friction angle grows from  $22.2^\circ$  to  $47.3^\circ$ , as the roughness increases from 0 mm to 2 mm. Owing to the incomplete drilling mud cleaning and relative low stiffness of sandstone, the internal friction angle of the sandstone–cement interface ( $25.9^\circ$ ) is much smaller than that of the shale–cement interface ( $37.9^\circ$ ).

Cohesive strength ( $c$ ) is the intercept of the fitted line, which represents the initial shear strength without the action of normal stress, and could be used to evaluate the initial bond strength of the rock–cement interface. As provided in Figure 10b, the cohesive strength shows a similar trend to the internal friction angle, but its change in range is relatively wider. Specifically, the values of cohesive strength decline from 5.87 MPa to 1.96 MPa, a drop of about 66.6%, as the surface cleanliness changes from fresh and untreated to drilling mud pollution without flushing, while it drops dramatically from 7.01 MPa to 0.89 MPa,

as the surface roughness decreases from 2 mm to 0 mm, which infers that the smooth wall of the wellbore does not have sufficient shear resistance. The cohesive strength of the sandstone–cement interface is only 0.72 MPa, much lower than that of the shale–cement interface (4.55 MPa).

**Table 5.** Data collection of shear stresses and calculated parameters of shear strength.

Sample Number	$\sigma_n$ (MPa)	$\tau_n$ (MPa)	$\tan\varphi$	$\varphi$ (°)	$c$ (MPa)	Linear Fit $\tau_n = \sigma_n \tan\varphi + c$
YS-2-0-1	6	11.34	0.8688	40.9	5.87	$\tau_n = 0.8688 \sigma_n + 5.87$ $R^2 = 0.9339$
YS-2-0-2	12	14.95				
YS-2-0-3	18	23.43				
YS-2-0-4	24	25.89				
YS-2-2-1	6	9.35	0.7788	37.9	4.55	$\tau_n = 0.7788 \sigma_n + 4.55$ $R^2 = 0.9930$
YS-2-2-2	12	13.45				
YS-2-2-3	18	19.08				
YS-2-2-4	24	23.05				
YS-2-3-1	4	4.05	0.5905	30.6	1.96	$\tau_n = 0.5905 \sigma_n + 1.96$ $R^2 = 0.9868$
YS-2-3-2	8	7.03				
YS-2-3-3	12	9.17				
YS-2-3-4	16	11.21				
YS-0-2-1	6	3.64	0.4071	22.2	0.89	$\tau_n = 0.4071 \sigma_n + 0.89$ $R^2 = 0.9843$
YS-0-2-2	12	5.39				
YS-0-2-3	18	8.07				
YS-0-2-4	24	10.89				
YS-4-2-1	4	12.08	1.0833	47.3	7.01	$\tau_n = 1.0833 \sigma_n + 7.01$ $R^2 = 0.9833$
YS-4-2-2	12	18.56				
YS-4-2-3	18	26.92				
YS-4-2-4	24	33.29				
SS-2-2-1	3	2.03	0.4863	25.9	0.72	$\tau_n = 0.4863 \sigma_n + 0.72$ $R^2 = 0.9878$
SS-2-2-2	6	3.79				
SS-2-2-3	9	5.24				
SS-2-2-4	12	6.41				

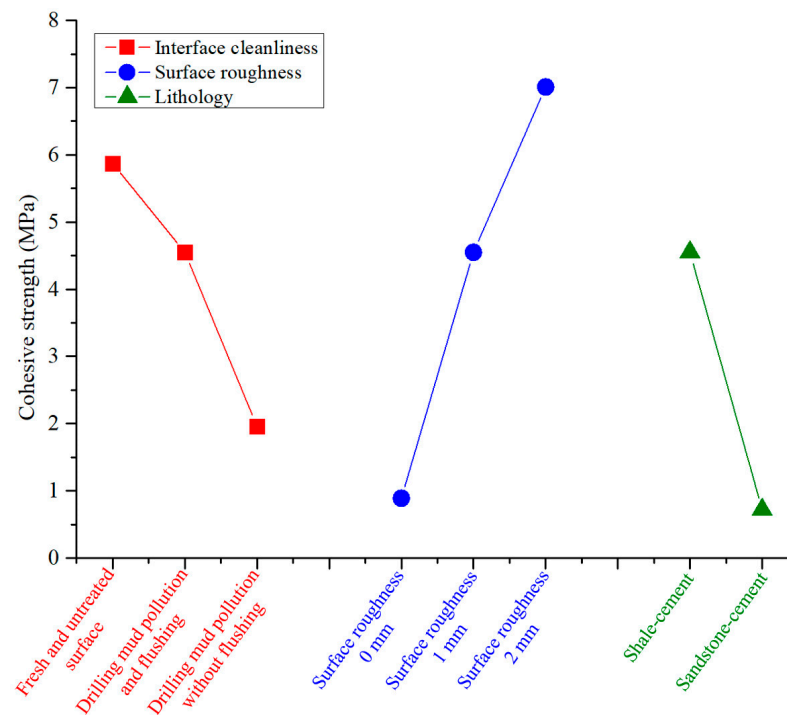
The analysis of shear fracture surface could provide detailed information about the failure mechanism. As shown in Figure 11, the shear fracture surface is not always exactly the rock–cement interface. It usually manifests as a shear zone, in which the rock, cement, and interface all contribute to the final shear failure. The morphology of fracture surface also shows diversity for different types of rock–cement specimens.

As shown in Figure 11a, the interface of composite specimens is fresh and uncontaminated with a roughness of 1 mm. The surfaces of the shear fractures are flat and exhibit gray friction trace, and we could not see the bumpy shale–cement interface, which are filled up and made even by the broken cement. All these indicate that shear failure mainly occurs in the cement part next to the interface. The reason is that when the shale and cement at the interface are firmly cemented, shear failure initiates and propagates along the relatively weak cement part. In addition, with the increase in normal stress, the friction trace becomes more significant.

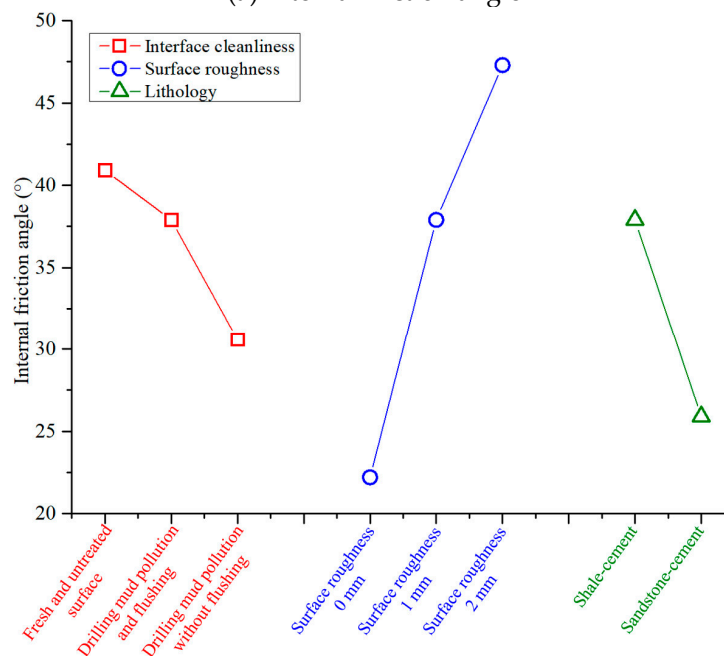
For specimens with interface treatment of drilling mud contamination and flushing fluid washing, shear failure still mainly happens in the cement part (Figure 11b). However, the surface of the shear fracture is no longer flat and shows certain roughness. As the residual drilling mud is not completely removed by flushing, and so the shale–cement interface is not cemented as firmly as that in the fresh state. During shear sliding, some cement, imbedded into the shale grooves, delaminates, so the surface becomes uneven.

As shown in Figure 11c, the interface is treated with drilling mud pollution without flushing. The surfaces of shear fractures are filled with residual drilling mud, and the

prefabricated corrugated undulation is clearly visible. Due to the residual drilling mud deposited in the grooves of shale surface, the effective cementation area is greatly reduced, and the interface is poorly cemented. When the normal stress reaches a relatively high level, the feature of friction sliding becomes more pronounced.



(a) Internal friction angle

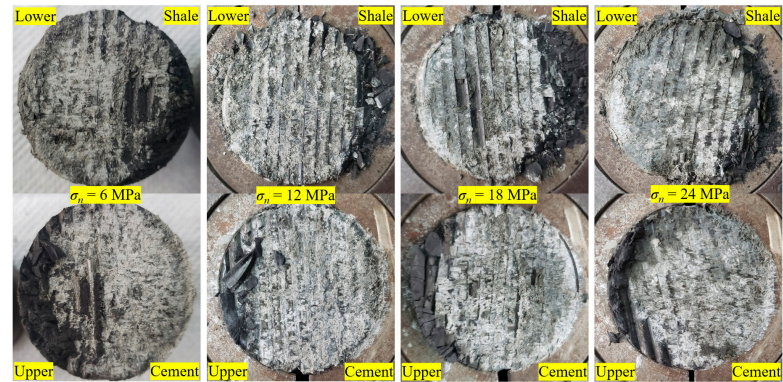


(b) Cohesive strength

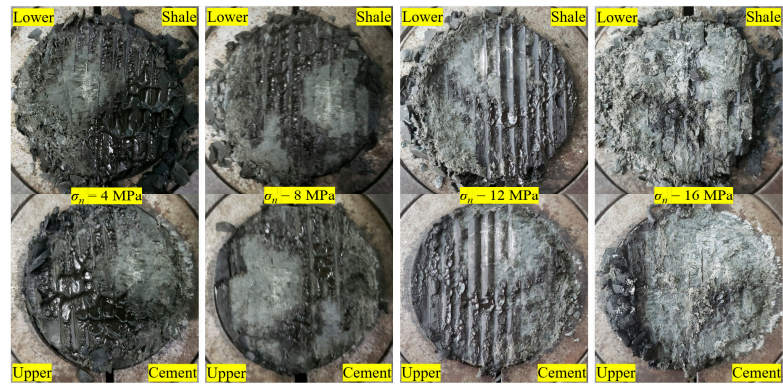
Figure 10. Variation of parameters of shear strength with different factors.



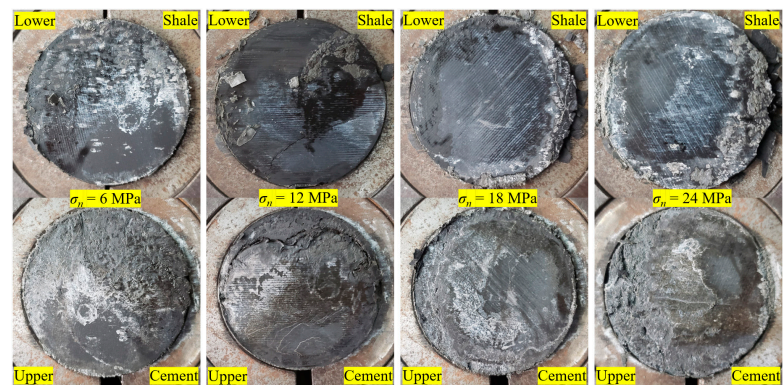
(a) YS-2-0-(1, 2, 3, 4)



(b) YS-2-2-(1, 2, 3, 4)

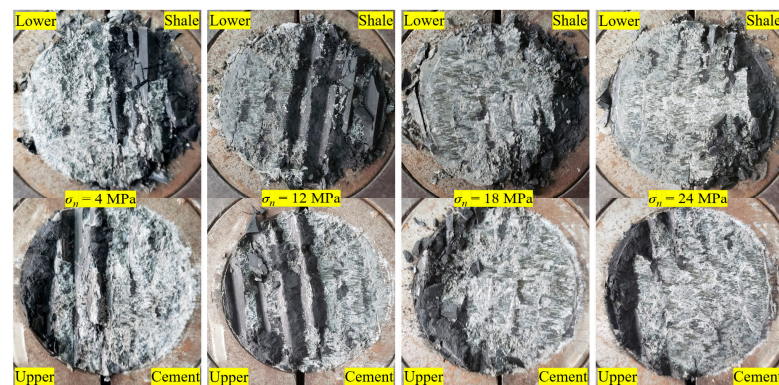


(c) YS-2-3-(1, 2, 3, 4)

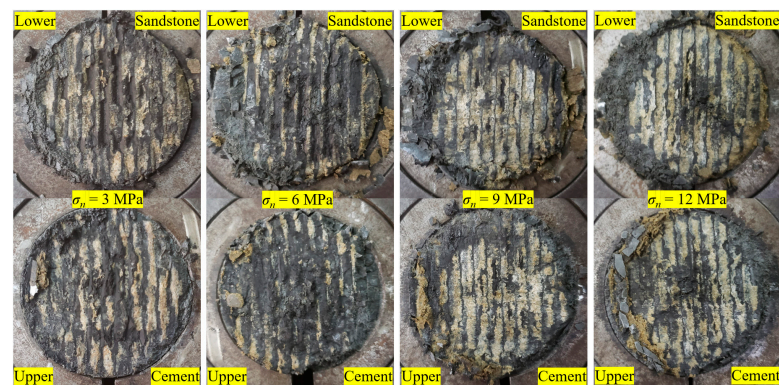


(d) YS-0-2-(1, 2, 3, 4)

Figure 11. Cont.



(e) YS-4-2-(1, 2, 3, 4)



(f) SS-2-2-(1, 2, 3, 4)

**Figure 11.** Morphology of shear fracture surfaces.

When the interface is flat, shear failure occurs exactly on the shale–cement interface (Figure 11d). A small amount of cement is still glued to the shale. Due to the flat surface and a little drilling mud residue, it is easy to start shear sliding, and the cohesive strength of the interface is relatively low.

Under the condition of large surface roughness (2 mm), the initiation and propagation of shale failure becomes more difficult. As shown in Figure 11e, because of the relatively large roughness, not only cement but also shale, participates in the formation of shear fractures. Consequently, the cohesive strength of this kind of interface is high and reaches 7.01 MPa.

As shown in Figure 11f, the shear fracture surface of sandstone–cement is mainly along the interface. Due to the poor flushing effect and low strength of the sandstone, residual drilling mud and fragments of sandstone and cement are seen on fracture surfaces.

## 4. Discussion

### 4.1. The Simulation of the Surface Roughness

It should be noted that directly observing the real internal wall of an underground open hole is not realistic. Therefore, the complete simulation of the irregularity of the real formation wall is very difficult. However, the observation of collected downhole full diameter cores help us understand the surface roughness of the wall. For the integral stratum, the collected cores are usually intact, and the surface of the cylinder sides are relatively smooth, with little roughness. The normal range of the interface roughness is usually 0~1 mm. For the formation with poor integrity, the drilling cores are broken, and the surface becomes rougher. The dimensions of hole collapse blocks could range from mm~cm.

#### 4.2. The Contribution of Rock Cohesion to the Interface Shear Failure

It is really difficult to precisely separate the contribution of the cohesion of shale or sandstone to the shear failure of the composite. However, a rough estimation can be made according to the failure mode around the interface. For instance, if the shale or sandstone at the interface remains relatively intact after shearing, we believe that the cohesion of the shale or sandstone does not participate in the shear failure. The shear parameters are also relatively small. Contrarily, if the bulges of the rock at the interface are broken during shearing, the cohesion of the rock contributes to the shear failure of the composite. The shear parameters could exhibit relatively high values.

#### 4.3. The Limitations

One of the primary objects of this research is to provide a methodology to investigate the compressive and shear mechanical properties of the cement–formation interface. The curing conditions were simply set at room temperature and atmospheric pressure. In the real underground environment, the cement slurry sets and hardens at certain temperatures and pressures, which grow with the increase in burial depth. The micro-structure and mechanical properties of the cement stone are sensitive to the curing environment. Therefore, more attention should be paid to the temperature and pressure of the curing period in future studies.

### 5. Conclusions

By considering the interface roughness and drilling mud residue in preparation of the cement–rock composite specimens, the compressive and direct shear tests were implemented. The flushing efficiency of the rock surface, compressive strength, interface incompatible deformation, shear strength parameters, and shear fracture morphology were described and analyzed. The conclusions are as follows:

- (1) With the shale surface roughness increasing from 0 to 2 mm, the flushing efficiency decreases from 76.7% to 64.2%. Under the same washing procedure, the flushing efficiency of sandstone is only 44.7%, remarkably lower than that of shale (68.7%);
- (2) In a uniaxial compression state, the compressive strength varies in a wide range (20.6~60.1 Mpa). Tensile splitting in a vertical direction is the dominate failure mode. The integrity of interface cementation depends on the interface cleanliness and roughness;
- (3) Under triaxial compression, all the stress–strain curves exhibit remarkable elastoplastic characteristics, and the compressive strength focuses on the range of 110~120 Mpa. The cement part presents noteworthy plastic deformation and several micro shear fractures develop. There is incompatible deformation between cement- and rock-induced interface debonding;
- (4) The internal friction angle and cohesive strength decrease with the increase in the degree of drilling mud pollution and increase with the rise in surface roughness. The shear failure surface usually manifests as a shear zone, in which the rock, cement, and interface all contribute to the final shear failure.

**Author Contributions:** Conceptualization, L.W. and Y.G.; data curation, L.W. and B.L.; formal analysis, L.W. and B.L.; funding acquisition, L.W. and H.L.; investigation, H.Y. and B.L.; project administration, Y.G. and J.L.; resources, Y.G. and H.L.; supervision, J.L. and Y.G.; validation, B.L. and H.Y.; writing—original draft, L.W.; writing—review and editing, B.L., H.Y., Y.G., J.L. and H.L. All authors have read and agreed to the published version of the manuscript.

**Funding:** This work was sponsored by the “National Natural Science Foundation of China” (No. 52104010), the “Sinopec Science and Technology Department Project” (No. P21056), the CAS Pioneer Hundred Talents Program (No. 2017-124).

**Institutional Review Board Statement:** Not applicable.

**Informed Consent Statement:** Not applicable.

**Data Availability Statement:** The data presented in this study are available on request from the corresponding author.

**Conflicts of Interest:** The authors declare no conflict of interest.

## References

1. Yin, F.; Hou, D.; Liu, W.; Deng, Y. Novel assessment and countermeasure for micro-annulus initiation of cement sheath during injection/fracturing. *Fuel* **2019**, *252*, 157–163. [[CrossRef](#)]
2. Gray, K.E.; Podnos, E.; Becker, E. Finite-element studies of near-wellbore region during cementing operations: Part I. *SPE Drill. Complet.* **2009**, *24*, 127–136. [[CrossRef](#)]
3. Li, J.; Xi, Y.; Tao, Q.; Li, Y.; Qu, G. Experimental investigation and numerical simulation of the emergence and development of micro-annulus in shale gas wells subjected to multistage fracturing. *J. Nat. Gas Sci. Eng.* **2020**, *78*, 103314. [[CrossRef](#)]
4. Fan, Z.; Parashar, R. Analytical Solutions for a Wellbore Subjected to a Non-isothermal Fluid Flux: Implications for Optimizing Injection Rates, Fracture Reactivation, and EGS Hydraulic Stimulation. *Rock Mech. Rock Eng.* **2019**, *52*, 4715–4729. [[CrossRef](#)]
5. Fan, Z.Q.; Jin, Z.H.; Johnson, S.E. Modelling petroleum migration through microcrack propagation in transversely isotropic source rocks. *Geophys. J. Int.* **2012**, *190*, 179–187. [[CrossRef](#)]
6. Zhang, N.; Shi, X.; Wang, T.; Yang, C.; Liu, W.; Ma, H.; Daemen, J.J.K. Stability and availability evaluation of underground strategic petroleum reserve (SPR) caverns in bedded rock salt of Jintan, China. *Energy* **2017**, *134*, 504–514. [[CrossRef](#)]
7. Lankof, L.; Tarkowski, R. Assessment of the potential for underground hydrogen storage in bedded salt formation. *Int. J. Hydrogen Energy* **2020**, *45*, 19479–19492. [[CrossRef](#)]
8. Raju, M.; Kumar Khaitan, S. Modeling and simulation of compressed air storage in caverns: A case study of the Huntorf plant. *Appl. Energy* **2012**, *89*, 474–481. [[CrossRef](#)]
9. Liu, W.; Zhang, Z.; Chen, J.; Jiang, D.; Wu, F.; Fan, J.; Li, Y. Feasibility evaluation of large-scale underground hydrogen storage in bedded salt rocks of China: A case study in Jiangsu province. *Energy* **2020**, *198*, 117348. [[CrossRef](#)]
10. Wang, T.; Yang, C.; Ma, H.; Li, Y.; Shi, X.; Li, J.; Daemen, J.J.K. Safety evaluation of salt cavern gas storage close to an old cavern. *Int. J. Rock Mech. Min. Sci.* **2016**, *83*, 95–106. [[CrossRef](#)]
11. Lavrov, A.; Torsæter, M. *Physics and Mechanics of Primary Well Cementing*; Springer International Publishing AG: Cham, Switzerland, 2016; ISBN 9783319431642.
12. Opedal, N.; Todorovic, J.; Torsæter, M.; Vrålstad, T.; Mushtaq, W. Experimental study on the cement-formation bonding. *SPE Eur. Form. Damage Conf. Proc. EFDC* **2014**, *1*, 227–238. [[CrossRef](#)]
13. Xu, H.; Ma, T.; Peng, N.; Yang, B. Influences of fracturing fluid injection on mechanical integrity of cement sheath under four failure modes. *Energies* **2018**, *11*, 3534. [[CrossRef](#)]
14. Xu, F.; Xu, Z.; Tang, S.; Ren, Q.; Guo, Y.; Wang, L.; Hou, Z.; Liu, Z. Evolution of physical and mechanical properties of cementing materials during underground energy exploitation and storage. *J. Energy Storage* **2022**, *45*, 103775. [[CrossRef](#)]
15. He, T.; Wang, T.; Xie, D.; Daemen, J.J.K. The mechanism of pores enhancing the deformation of completion cement under confining pressure. *Cem. Concr. Compos.* **2022**, *125*, 104322. [[CrossRef](#)]
16. Quercia, G.; Chan, D.; Luke, K. Weibull statistics applied to tensile testing for oil well cement compositions. *J. Pet. Sci. Eng.* **2016**, *146*, 536–544. [[CrossRef](#)]
17. Wang, L.; Zeng, Y.; Zhang, Q.; Xu, F.; Yang, C.; Guo, Y.; Tao, Q.; Liu, J. Experimental study on mechanical properties of oil well cement under high temperature. *J. China Univ. Pet. Ed. Nat. Sci.* **2018**, *42*, 88–95. [[CrossRef](#)]
18. Li, Z.; Sun, J.; Luo, P.Y.; Lin, L.; Deng, Z.; Guo, X. Research on the law of mechanical damage-induced deformation of cement sheaths of a gas storage well. *J. Nat. Gas Sci. Eng.* **2017**, *43*, 48–57. [[CrossRef](#)]
19. Ladva, H.K.J.; Craster, B.; Jones, T.G.J.; Goldsmith, G.; Scott, D. The cement-to-formation interface in zonal isolation. *SPE Drill. Complet.* **2005**, *20*, 186–197. [[CrossRef](#)]
20. Plank, J.; Tiemeyer, C.; Buelichen, D. A study of cement/mudcake/formation interfaces and their impact on the sealing quality of oilwell cement. In Proceedings of the IADC/SPE Asia Pacific Drilling Technology Conference, Bangkok, Thailand, 25–27 August 2014. [[CrossRef](#)]
21. Liu, X.; Nair, S.D.; Cowan, M.; Van Oort, E. A novel method to evaluate cement-shale bond strength. In Proceedings of the SPE International Symposium on Oilfield Chemistry, The Woodlands, TX, USA, 13 April 2015.
22. Lian, W.; Li, J.; Liu, G.; Tao, Q. Numerical simulation of cement-to-formation interface debonding during hydraulic fracturing of shale gas wells. *J. Adhes. Sci. Technol.* **2020**, *34*, 917–935. [[CrossRef](#)]
23. Zhou, J.; Zeng, Y.; Guo, Y.; Chang, X.; Liu, L.; Wang, L.; Hou, Z.; Yang, C. Effect of natural filling fracture on the cracking process of shale Brazilian disc containing a central straight notched flaw. *J. Pet. Sci. Eng.* **2021**, *196*, 107993. [[CrossRef](#)]
24. Zhou, X.; Liu, H.; Guo, Y.; Wang, L.; Hou, Z.; Deng, P. An evaluation method of brittleness characteristics of shale based on the unloading experiment. *Energies* **2019**, *12*, 1779. [[CrossRef](#)]
25. Yang, H.; Guo, Y.; Wang, L.; Bi, Z.; Guo, W.; Zhao, G.; Yang, C. Study on the Stimulation Effectiveness Evaluation of Large-Scale Hydraulic Fracturing Simulation Experiment Based on Optical Scanning Technology. *SPE J.* **2022**, 1–19. [[CrossRef](#)]
26. Heng, S.; Guo, Y.; Yang, C.; Daemen, J.J.K.; Li, Z. Experimental and theoretical study of the anisotropic properties of shale. *Int. J. Rock Mech. Min. Sci.* **2015**, *74*, 58–68. [[CrossRef](#)]

- 
27. Jaeger, J.C.; Cook, N.G.W.; Zimmerman, R.W. *Fundamentals of Rock Mechanics*, 4th ed.; Blackwell Publishing: Oxford, UK, 2007; ISBN 9788578110796.
  28. Wang, L.; Guo, Y.; Yang, C.; Xiao, J.; Lu, C.; Song, Y. Mechanical characterization of continental shale in Sichuan Basin of China and its potential impact on reservoir stimulation. *J. Nat. Gas Sci. Eng.* **2020**, *79*, 103346. [[CrossRef](#)]